Interplay between thermal Rydberg gases and plasmas

Daniel Weller,[1] James P. Shaffer,[2] Tilman Pfau,[1] Robert Löw,[1] and Harald Kübler[1,*]

[1]*5. Physikalisches Institut and Center for Integrated Quantum Science and Technology, University of Stuttgart, Pfaffenwaldring 57, D-70569 Stuttgart, Germany*

[2]*Quantum Valley Ideas Laboratories, 485 Wes Graham Way, Waterloo, Ontario N2L 0A7, Canada*

We investigate the phenomenon of bistability in a thermal gas of cesium atoms excited to Rydberg states. We present both measurements and a numerical model of the phenomena based on collisions. By directly measuring the plasma frequency, we show that the origin of the bistable behavior lies in the creation of a plasma formed by ionized Rydberg atoms. Recombination of ions and electrons manifests as fluorescence which allows us to characterize the plasma properties and study the transient dynamics of the hysteresis that occurs. We determine scaling parameters for the point of plasma formation, and verify our numerical model by comparing measured and simulated spectra. These measurements yield a detailed microscopic picture of ionization and avalanche processes occurring in thermal Rydberg gases. From this set of measurements, we conclude that plasma formation is a fundamental ingredient in the optical bistability taking place in thermal Rydberg gases and imposes a limit on usable Rydberg densities for many applications.

I. INTRODUCTION

Highly excited atoms are well known for their extraordinary properties, such as high sensitivity to electric fields and strong interactions between Rydberg atoms effective in the micrometer range. These properties can be fine-tuned by choosing different Rydberg states. The strong long-range interactions between Rydberg atoms has motivated studies of a variety of collective phenomena and applications with strongly correlated atomic clouds. Among some of the most prominent in the field of ultracold atoms are quantum gates [1,2], quantum phase transitions [3,4], optical nonlinearities on the single photon level [5–9], beyond two-body interactions [10], excitation transfer [11,12], aggregation of excitations [13–15], and ultralong-range molecules [16,17]. The study of Rydberg atoms in thermal vapors enriches the spectrum of research topics as these vapors can provide much larger atom numbers and higher densities compared to ultracold gases. Besides this, the technical overhead for hot vapor spectroscopy is much smaller and it does not require preparation steps such as laser and evaporative cooling. The possibility to work at high bandwidths and fast time scales brings this technology closer to real world applications. Examples of these areas of focus are electric field and terahertz sensing [18,19] and single photon sources [20].

One of the topics that has generated interest in hot Rydberg atom physics is the phenomenon of optical bistabilities [21–26]. The mechanism that is responsible for the observation of bistability in Rydberg gases has been controversial as charged particles and long-range Rydberg atom interactions can, in principle, both lead to bistable behavior.

In our previous publication [26] we presented experimental evidence that the underlying mechanism for the optical bistability is given by the presence of charges in the vapor. However, a minute picture remains to be worked out. In this article, we show that the appearance of optical bistability in a thermal Rydberg vapor is caused by a plasma that is formed due to inelastic, ionizing collisions between Rydberg atoms and ground-state atoms which generate charged particles. The electrons produced by the ionization of the Rydberg atoms become an additional source for collisions with Rydberg atoms leading to even more charges in the system. Eventually, when sufficiently many Rydberg atoms are ionized, a steady-state plasma is formed. We explore the relation between the Rydberg density, the plasma charge density, and the plasma frequency by directly measuring the interaction of the plasma with a radio-frequency field. We introduce a model for the steady state of the system based on the excitation of Rydberg states and their subsequent ionization due to collisions. With this model we are able to determine two scaling parameter (one for each scan direction of the excitation lasers) such that the point of plasma formation is described by a simple linear function. The theoretical model is compared to experimental spectra and excellent agreement is found. We conclude that the underlying mechanism for the optical bistability in thermal Rydberg gases is dominated by the formation of a plasma, which acts back on the Rydberg excitation via the Stark effect.

The interplay between Rydberg density and the presence of a plasma has important implications on every thermal vapor cell experiment that involves Rydberg atoms when laser intensities are outside the weak probe regime. The presence of charged particles in the vapor alters the value of the electric dipole matrix elements of the atoms and allows for the admixture of dipole-forbidden transitions. This directly affects the pair potentials of Rydberg-Rydberg interactions and therefore influences any blockade/antiblockade physics
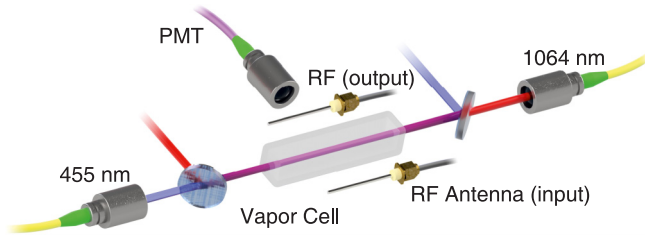
FIG. 1. Experimental setup. Two counterpropagation laser beams excite the Cs atoms in a vapor cell to a Rydberg state. The change in the radio-frequency transmission through the atomic sample is measured with the dipole antennas shown in the figure. The atomic fluorescence is captured with a fiber, bandpass-filtered, and detected on a PMT.
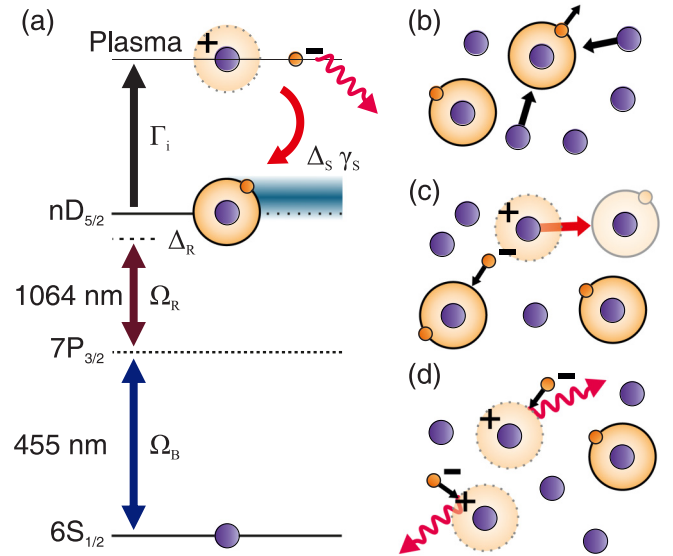

FIG. 2. (a) Three-level diagram for optical excitation with ionization to an additional plasma state. The plasma causes a shift and broadening of the Rydberg level, and recombination results in fluorescence. (b) and (c) Illustration of the processes leading to plasma formation and bistability, as described in Sec. III. (b) Rydberg-ground-state collisions ionize some atoms leading to production of fast electrons. (c) Avalanche ionization due to fast electrons and broadening due to steep electric field gradients can facilitate higher Rydberg population. (d) Fluorescence due to recombination in the plasma.

as well as Rydberg dressing. As the electric field is not homogeneous but given by a distribution, the field gradients lead to shorter coherence times and time-varying interactions. Especially continuous beam experiments suffer from this limitation, but also pulsed experiments are imposed by an upper boundary with respect to the repetition rate and pulse duration. Understanding the microscopic mechanisms that are responsible for ion production and its corresponding electric field distribution in thermal Rydberg vapor is an important component for future experiments and applications.

The paper is organized in six sections. In Sec. II we describe the experimental setup and conditions under which we performed the measurements. We qualitatively describe the microscopic model that captures the underlying mechanisms responsible for the observed phenomenon of optical bistability in Sec. III. Section IV presents the data showing that a plasma is present in the thermal Rydberg gas. Based on collisional cross sections and motional dephasing in an electric field distribution, we have developed a microscopic model which is detailed in Sec. V. We confirm our model by comparing measured and simulated data before concluding the manuscript with Sec. VI.

II. SETUP AND METHODS

Figure 1 shows the experimental setup for the investigation of the origin of the bistability and the analysis of the plasma. A vapor cell containing cesium is placed in the path of two counterpropagating, collimated laser beams. Each beam has a $1/e^2$ radius of 0.7 mm. The vapor cell has a square cross section with a side length of 1 cm. The length in the direction along the beam is 5 cm. The bulk of the cesium resides in a reservoir attached to a side arm of the vapor cell. The temperature of the reservoir is stabilized to control the vapor density inside the vapor cell. The main body of the vapor cell is held at a higher temperature to prevent alkali condensation on the windows. We determine the cesium atomic density for each measurement by recording and fitting the absorption profile of the cesium D_2 spectrum [27]. The densities used for the experiments are varied from 5×10^{10} cm^{-3} to 7×10^{12} cm^{-3}.

We excite Cs atoms to the $nD_{5/2}$ Rydberg state ($n = 30$ and 42) via the inverted wavelength two-photon scheme depicted in Fig. 2(a). The first laser is a frequency-stabilized 455-nm laser—a frequency doubled diode laser—tuned to

the cesium $6S_{1/2}, F = 3 \rightarrow 7P_{3/2}, F' = 4$ transition. Rabi requencies, $\Omega_B/2\pi$, used for the experiments range between 1 and 12 MHz. The 455-nm laser is locked via dichroic atomic vapor spectroscopy [28] in a separate cesium vapor cell. The second laser—a fiber-amplified 1064-nm diode laser—is either scanned over the cesium $7P_{3/2} \rightarrow nD_{5/2}$ transition with a detuning Δ_R (measurements with $n = 42$), or locked on resonance (measurements with $n = 30$), using another cesium vapor cell. Side-of-fringe locking [29] to the reference electromagnetically induced transparency (EIT) signal is used for this light field [30]. Rabi frequencies, $\Omega_R/2\pi$, are varied between 3 and 90 MHz. The laser detuning scans are calibrated using a Fabry-Pérot interferometer with a free-spectral range of $\Delta\nu_{FSR} = 1$ GHz in combination with an EIT reference signal.

The fluorescence from the highly excited atoms was used to identify the formation of the plasma. Due to the high laser powers involved, measured changes in the transmission of either light field suffer from a large background signal. For this reason, we either measure the change in transmission of a radio-frequency field (frequency f_{RF} ranging from 8 to 300 MHz) through the vapor cell in the presence of Rydberg excitations and ions, or the change in fluorescence to obtain a signal. Long- and short-pass filters are placed in front of a photomultiplier tube (PMT) with a bandwidth of 20 kHz so that the fluorescence light between 500 and 800 nm transverse to the laser beam propagation direction can be collected. With this interval, we exclude the 455-nm laser light, and the strongly fluorescing decay via the D2 line at 852 nm that

can already occur with the 455-nm excitation on its own. The fluorescence is collected by an imaging system consisting of two lenses with focal lengths of $f_1 = 30$ mm and $f_2 = 8$ mm. The second lens focuses the light into a multimode fiber, 400-μm core diameter. The fluorescence is imaged onto the fiber facet from within the excitation laser beam path, which is about 45 mm in front of the first lens. The diameter of the spot from which photons are collected is approximately 1.5 mm. Overall, we estimate that the collection efficiency is $\sim 0.1\%$ of the photons emitted into all directions from that spot.

For the transmission measurements of the radio-frequency fields, the RF field is coupled into the vapor cell with a 4-cm-long dipole antenna that is oriented parallel to the laser beams. A second, identical antenna at the opposite side of the vapor cell picks up the signal. In some measurements, to appear later in the paper, we measure the atomic fluorescence as a surrogate for the microwave transmission measurements. We show that this proxy is a valid one. In order to improve the signal-to-noise ratio, we modulate the radio-frequency amplitude as well as the laser intensity and make use of lock-in amplification. We used two lock-in steps in combination with quadrature detection.

III. BISTABILITY MECHANISM

In previous work on optical bistability in thermal vapor cells the authors assumed that mutual Rydberg atom interactions embody the mechanism. The effect of charges was not incorporated into the model used to explain the observed behavior [21,23,24]. The term *optical bistability*, in the context of Rydberg atoms and plasmas in thermal vapor cells, refers to the appearance of a hysteresis in the observed spectral response of the system when scanning one laser in a multiphoton excitation scheme across a Rydberg state resonance. The hysteresis arises due to the competition between a nonlinear shift—in our case caused by a Stark shift due to surrounding charges—on the one side and decay of the excited state population on the other side.

Figure 3(a) shows a photograph of the vapor cell from the side. The beams travel horizontally through the cell. Given suitable combination of density, laser power, and detuning; The lasers create a fluorescing ray [Figs. 3(b)–3(d)], consistent with the spectra reported in [21]. As the 1064-nm laser is scanned back and forth across the Rydberg resonance position, fluorescence suddenly appears to streak across the vapor cell for one scan direction, but then gradually retracts towards the entrance window of the blue laser beam until it completely vanishes for the opposite scan direction. The directionality of the phenomenon depends on the sign of the polarizability. This *lightsaber* like phenomenon [31] with a distinct transition between a light and a dark side along the beam [Figs. 3(b)–3(d)] repeats for every cycle of the detuning scan, and is visible by eye. This is a visual manifestation of the optical bistability.

In this work, we modify the overall concept for the occurrence of the hysteresis as depicted in Fig. 2. As evidenced in [26], charges play an essential role in the optical bistability that takes place in dense thermal Rydberg gases. In fact, it is not Rydberg-Rydberg interactions that mediate the optical bistability, but the plasma of ions and electrons that are created
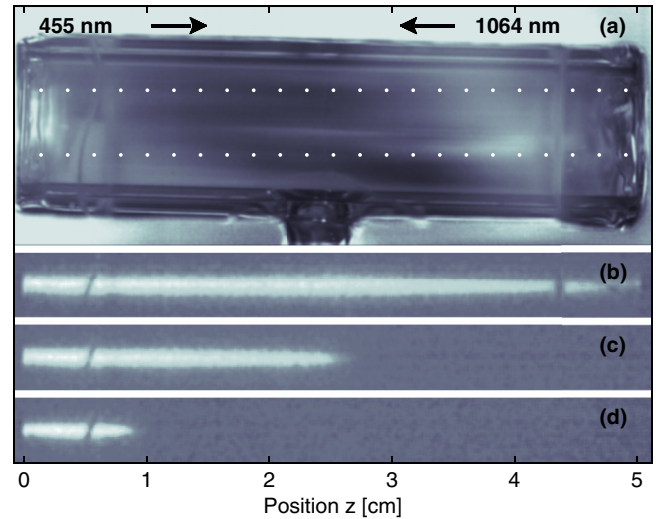

FIG. 3. (a) Side view of the cell. The lasers propagate between the dotted lines; 455-nm laser from left to right, 1064-nm laser from right to left. (b)–(d) Fluorescence image for wavelengths between 500 and 800 nm with background subtracted. Scanning the Rydberg laser across resonance creates a *lightsaber* like fluorescing ray. When appearing, the glowing beam extends across the whole cell at once (b), and then gradually retracts from right to left as the detuning is scanned (c) and (d), before smoothly vanishing completely. The 455-nm laser intensity decreases from left to right due to absorption. At the transition between light and dark side, the conditions for plasma formation are not fulfilled any further along the beam. The defects on the left- and right-hand side are due to quartz sublimate on the surface of the cell. The position z along the cell is indicated on the bottom axis.

at the Rydberg densities required to observe the effect. We show that in typical optical bistability experiments over a range of parameters where the phenomena can be observed, a weakly coupled plasma exists in the vapor. The sudden switching to the plasma state via an avalanche ionization process leads to the observation of the hysteresis that motivates the term optical bistability. Here, the term bistability is used in that sense that the system jumps from one metastable state to another via this avalanche dynamics [32]. We have identified two mechanisms that contribute to the ionization initiating the plasma formation. Rydberg atoms collide with ground-state atoms [Fig. 2(b)], creating ions and free electrons. The electrons then collide with other Rydberg atoms [Fig. 2(c)], giving rise to a much higher ionization rate Γ_{i}. This effect is commonly known as the *avalanche process* [33–35].

The plasma plays a fundamental role in the bistability observed in the thermal Rydberg gas. With charges present in the gas, the Rydberg energy level is shifted due to the Stark shift Δ_{S}. As thermal atoms move through an electric field distribution [36], their energy levels rapidly change during the atom-light interaction causing a homogeneous broadening. Therefore, an additional dephasing γ_{S} of the Rydberg population needs to be taken into account [37] which changes the excitation dynamics of the driven system. Plasma recombination gives rise to the distinct fluorescence spectrum [19,21,38]
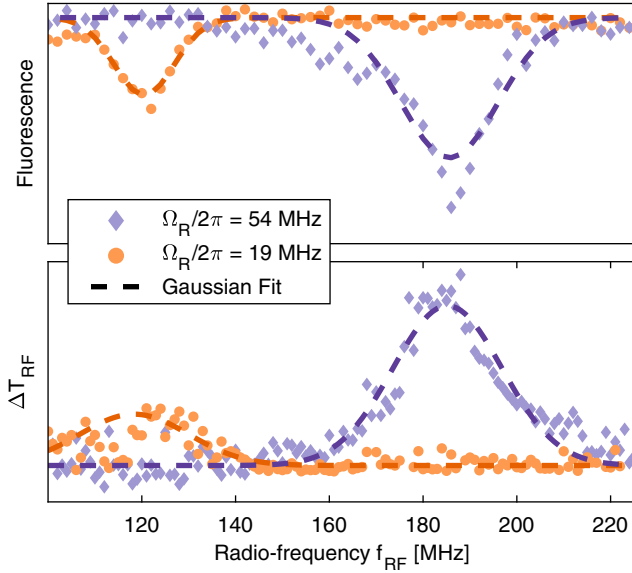
FIG. 4. Fluorescence vs radio-frequency (top) and radio-frequency transmission change (bottom) for the $30D_{5/2}$ Rydberg state for the same experimental conditions, with both lasers locked. Experimental parameters are $P_{RF} = -15$ dBm, $\Omega_B/2\pi = 3.6$ MHz, and $\mathcal{N}_g = 3 \times 10^{12}$ cm^{-3}. The dashed lines are Gaussian fits.

which can be measured. The recombination events lead to a broad, discrete distribution of Rydberg principal quantum number states which then subsequently decay [Fig. 2(d)].

IV. PLASMA CHARACTERIZATION

We measured the change in transmission ΔT_{RF} of a radio-frequency signal to show that a plasma exists in the gas. The results are shown in Fig. 4. The resonance position and its shift with the Rydberg density already suggests the presence of an (electron) plasma. The effect of the radio-frequency excitation would not occur in a neutral cesium gas at these frequencies. The data set was taken for two different Rydberg excitation laser Rabi frequencies Ω_R, but otherwise identical configurations. Both lasers were locked on resonance and excite the atoms to the $30D_{5/2}$ state. The ground-state cesium density was $\mathcal{N}_g = 3 \times 10^{12}$ cm^{-3} and the radio-frequency power delivered to the antenna was $P_{RF} = -15$ dBm.

A careful look at Fig. 4 appears puzzling at first glance since the radio-frequency field doesn't appear in absorption but increased transmission. The enhanced coupling between the two antennas is justified by the increased electric susceptibility, $\epsilon > 1$, and the fact that the antennas are in the near field of each other. Effectively, the distance between the antennas is being reduced by the free charges within the plasma.

Figure 4 additionally shows the change in fluorescence measured as a function of radio frequency f_{RF}. The overlap of the radio-frequency and fluorescence signals shows that the fluorescence can be used as a surrogate for the radio-frequency transmission signal. Such a connection is important because the fluorescence signal has a much larger signal-to-noise ratio than the radio-frequency transmission signal and therefore easier and much faster to measure. The change in fluorescence can be explained by considering how
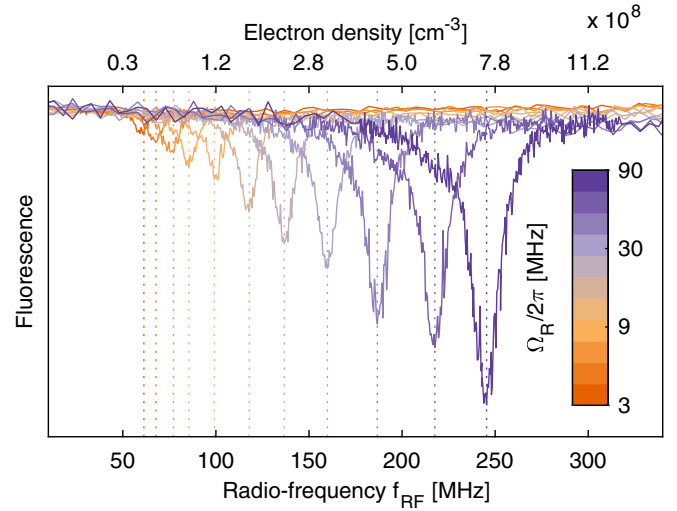

FIG. 5. Plasma resonance peaks in the fluorescence signal. Experimental parameters are as follows: radio-frequency power $P_{RF} = -16$ dBm, density $\mathcal{N}_g = 3 \times 10^{12}$ cm^{-3}, $\Omega_B/2\pi = 3.6$ MHz. The $30D_{5/2}$ Rydberg state was used for the measurements.

the radio-frequency field accelerates the free electrons into an oscillating motion with an amplitude depending on the frequency of the radio-frequency field. If the radio-frequency field is resonant with the plasma frequency, the amplitude of the electron oscillation is maximal and the motion effectively decreases the electron density within the laser beams. If the amplitude of the electrons exceeds the radial extent of the laser beams, the recombination probability in the center of the beam, where the ions are presumably located and most fluorescence is collected, decreases. The electrons can also collide with the walls of the vapor cell, further reducing the number of particles contributing to the fluorescence signal.

Figure 5 shows a typical series of measurements with varying Rydberg excitation laser intensity. As the Rabi frequency Ω_R gradually increases, the plasma resonance clearly shifts its position and increases in amplitude. The shift in the plasma resonance enables us to extract the density of the electron plasma. Given the relation between plasma frequency f_p and the electron density $\mathcal{N}_e$,

$$\mathcal{N}_e = (2\pi f_p)^2 \frac{\epsilon_0 m_e}{q_e^2}, \tag{1}$$

the electron density can be calculated using the electron mass m_e, the electronic charge q_e, and the permittivity of free space ϵ_0. The axis ticks above Fig. 5 are computed with this formula, yielding an electron density on the order of 1×10^8 cm^{-3}. Note that the observed plasma resonance in Fig. 5 must be that of the electrons because a calculation of the ion density using these resonant frequencies gives densities that are 2–100 times larger than the peak cesium vapor density $\mathcal{N}_g = 3 \times 10^{12}$ cm^{-3} we measured in the vapor cell.

Along with the plasma frequency, the Debye length,

$$\lambda_D = \sqrt{\frac{\epsilon_0 k_B T}{\mathcal{N}_e q_e^2}}, \tag{2}$$
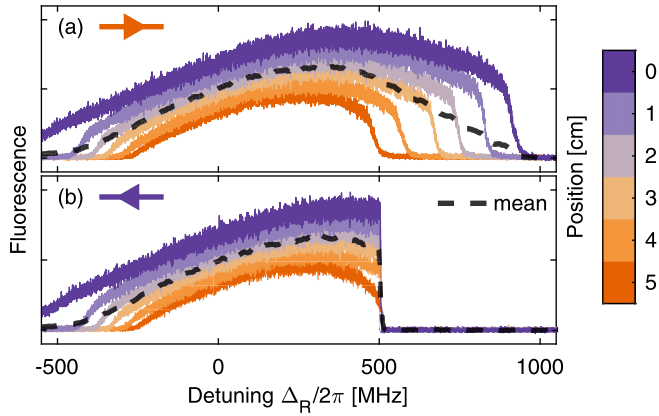
FIG. 6. Fluorescence signal collected from different spatial positions along the vapor cell, with increasing distance from the entrance window of the blue laser beam. (a) Scan from red to blue detuning (i.e., left to right). (b) Scan from blue to red detuning. All traces in (b) feature the same sharp edge at approximately 500 MHz. The dashed line shows the mean of the fluorescence signal. The mean is similar to the integrated signal one would obtain by measuring the probe transmission, e.g., as in [21,26]. Experimental parameters are $\mathcal{N}_\mathrm{g} = 3 \times 10^{12}\,\mathrm{cm}^{-3}$, $\Omega_\mathrm{B}/2\pi = 2.5\,\mathrm{MHz}$, and $\Omega_\mathrm{R}/2\pi = 18\,\mathrm{MHz}$. Data is shown for the $42D_{5/2}$ Rydberg state.

and the Coulomb coupling parameter,

$$\Gamma_e = \frac{q_\mathrm{e}^2}{4\pi\epsilon_0 k_\mathrm{B} T} \sqrt[3]{\frac{4\pi\mathcal{N}_\mathrm{e}}{3}}, \qquad (3)$$

fully describe the plasma. Assuming a plasma temperature equal to the vapor temperature $T = 370\,\mathrm{K}$, the Debye length is $\lambda_\mathrm{D} \sim 100\,\mu\mathrm{m}$ and the Coulomb coupling parameter is $\Gamma_e \sim 0.006$. k_B is the Boltzmann constant. The plasma parameters indicate that the electron plasma is in the weakly coupled regime. The associated plasma parameter,

$$N_\mathrm{D} = \mathcal{N}_\mathrm{e} \tfrac{4}{3}\pi \lambda_\mathrm{D}^3, \qquad (4)$$

which is the number of electrons in a Debye sphere, is $N_\mathrm{D} = 10^3$. The volume of the Debye sphere contains 1.3×10^7 Cesium atoms. The plasma is weakly ionized and has properties comparable to the earth's ionosphere [39].

Figure 6 shows a set of fluorescence signal data for both red to blue and blue to red 1064-nm laser scans at different fluorescence collection positions z along the vapor cell. The fluorescence is associated with population in a large number of Rydberg states because of recombination. The fluorescence was dispersed with a spectrometer to verify that a broad distribution of Rydberg states were present. As evident from the plots, the system stays in the state with a high Rydberg density [40] when scanning from red towards blue detuned wavelengths, even for larger detunings, Fig. 6(a). The behavior of the curves in Fig. 6(a) is to be contrasted with that in Fig. 6(b) where a sharp transition occurs at the same 1064-nm laser detuning for all fluorescence collection points.

It is apparent that for larger distances from the 455-nm laser beam input window, corresponding to larger propagation distances of the blue light through the vapor cell, the overall strength of the fluorescence signal decreases. The decreasing 455-nm laser intensity affects the detuning at which the

falling edge of the hysteresis occurs for red to blue detuning, Fig. 6(a). In contrast, the plots in Fig. 6(b) all feature the same sharp edge at approximately 500 MHz. The rising edge, Fig. 6(b), where the data is acquired for blue to red detuning, is unaffected by the varying 455-nm laser absorption along the length of the vapor cell. When the system is in the bistable part of the spectrum, but in the low Rydberg population state, the conditions for the ionization only need to be fulfilled at a single position along the laser beam. The avalanche ionization then quickly spreads across the whole cell. We estimate the time scale to be on the order of 10 ms. Typically, the conditions for the avalanche ionization are fulfilled first where the maximum Rabi frequency Ω_B exists, i.e., at the entrance window of the blue laser.

The prominent jump in the Rydberg population and associated change in fluorescence is referred to as the *edge frequency*. In the numerical evaluation of the data, we determine the edge frequency as the 1064-nm laser detuning value Δ_E, where the fluorescence signal exceeds $1/4$ of the maximum value in each trace, when tracing the data from the blue side. It is useful to look at Δ_E to determine how the laser Rabi frequencies and density scale with its value in order to learn about the driven system dynamics.

The plasma and its role in bistability can be further analyzed by investigating the dependence on the laser Rabi frequencies and vapor density. To study the optical bistability the 1064-nm laser is scanned across the $7P_{3/2} \rightarrow 42D_{5/2}$ transition. We collected the fluorescent light as described in Sec. II. Since the system is bistable, both positive and negative scan directions are recorded and treated separately. We measured spectra for a wide range of experimental parameters, varying vapor density and both excitation laser Rabi frequencies, Ω_B and Ω_R. We focused on analyzing the transition to the plasma state as we sweep the 1064-nm laser detuning across the spectrum. We show that it is possible to combine the experimental parameters into two scaling parameters S or $S^\star$, for the blue to red scan and red to blue, respectively. The scaling parameter S and $S^\star$ are defined as

$$S^{(\star)} = \left(\frac{\mathcal{N}_\mathrm{g}}{\mathcal{N}_0}\right)^a \cdot \left(\frac{\Omega_\mathrm{B}^{(\star)}}{\Omega_0}\right)^b \cdot \left(\frac{\Omega_\mathrm{R}}{\Omega_0}\right)^c. \qquad (5)$$

The two sets of exponents (a, b, c) are chosen in such a way that the frequencies where the system jumps between high and low Rydberg excitation linearly scale with $S^\star$ or S. The asterisk denotes that the Rabi frequency is *adjusted* for absorption up to the position where the fluorescence measurement is made; see Appendix A. Previous experiments demonstrate that the frequency shift of the phase transition additionally scales with the fourth power of the effective principal quantum number $n^{\star 4}$ [24]. This is consistent with our interpretation, because the geometric cross section of Rydberg atoms for ionizing collisions also scales with $n^{\star 4}$.

The set of data points we acquired for the bistability edge position are plotted in Fig. 7. The plots cover $\Omega_\mathrm{B}/2\pi$ over a range of 1–12 MHz, $\Omega_\mathrm{R}/2\pi$ from 15 to 50 MHz, and $\mathcal{N}_\mathrm{g}$ within $5 \times 10^{10}\,\mathrm{cm}^{-3}$ to $7 \times 10^{12}\,\mathrm{cm}^{-3}$.

The values for the three scaling exponents (a, b, c) are obtained by a nonlinear least-squares fit to the data plotted in Fig. 7, for each scan direction. The results are given in Table I.
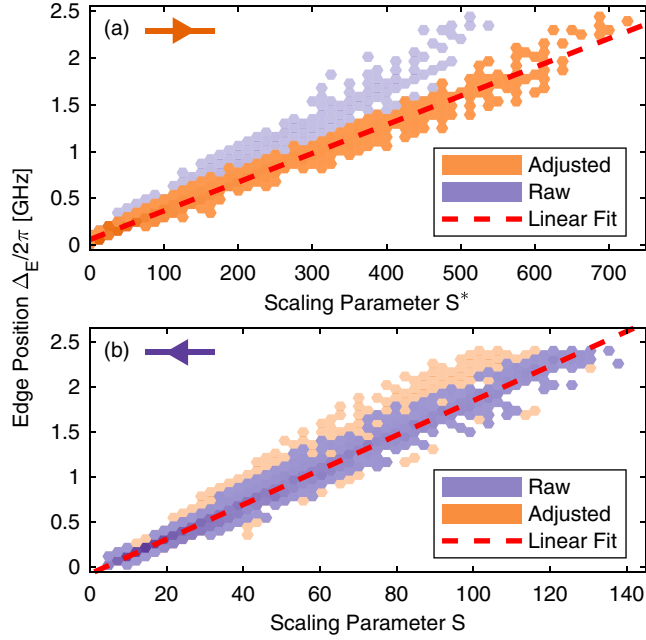
FIG. 7. Map of the bistability frequency edge Δ_E as a function of the scaling parameters S and $S^\star$, according to Eq. (5). (a) Red to blue detuning. (b) Blue to red detuning. For comparison, the larger spread of the distributions with the respective raw and absorption adjusted Rabi frequencies are shown.

The fact that the values are different for S and $S^\star$ indicates that the dynamics are different for the two detuning cases as is expected for bistable behavior.

Interpreting the numerical values of the exponents for the scaling parameters reveals interesting properties of the bistable system. An intuitive picture based on rate equations can be developed, to explain the rough trend of the determined exponents (a, b, c). The most important parameters are the density of Rydberg atoms and ions, $\mathcal{N}_{Ryd}$ and $\mathcal{N}_{ion}$. The two steady-state densities can be obtained by solving the coupled system of rate equations,

$$\dot{\mathcal{N}}_{ion} = \mathcal{N}_{Ryd}\mathcal{N}_g\sigma_g\overline{v} + \mathcal{N}_{Ryd}\mathcal{N}_{ion}\sigma_e\overline{v}'$$
$$- \mathcal{N}_{ion}\mathcal{N}_e\sigma_r\overline{v}'' - \mathcal{N}_{ion}\Gamma_t,$$
$$\dot{\mathcal{N}}_{Ryd} = -\mathcal{N}_{Ryd}\mathcal{N}_g\sigma_g\overline{v} - \mathcal{N}_{Ryd}\mathcal{N}_{ion}\sigma_e\overline{v}' + \mathcal{R}_{pump}. \quad (6)$$

The cross sections for Rydberg-ground-state collisions σ_g, Rydberg-electron collisions σ_e, and recombination of ions with electrons σ_r and mean relative velocity $\overline{v}$ of the respective interacting species are parameters in these equations. Ions diffuse away at a rate Γ_t. The effective rate at which atoms are excited to the Rydberg state is $\mathcal{R}_{pump}$. The decay of the Rydberg population results in an offset in the resulting equa-

TABLE I. Scaling exponents as in Eq. (5) with 95% confidence intervals.

	(Scan)	a ($\mathcal{N}_g$)	b (Ω_B)	c (Ω_R)
S	($\leftarrow$)	0.81 ± 0.01	0.95 ± 0.02	1.08 ± 0.02
$S^\star$	($\rightarrow$)	0.54 ± 0.01	0.56 ± 0.01	0.97 ± 0.02

tions, and does not play a role for the scaling behavior in the parameters of interest. Depending on whether the system approaches Δ_E from the ground-state side ($\mathcal{N}_{ion}, \mathcal{N}_e, \mathcal{N}_{Ryd} \approx 0\,cm^{-3}$) or the highly populated excited state side ($\mathcal{N}_{ion}, \mathcal{N}_e, \mathcal{N}_{Ryd} \gg 0\,cm^{-3}$), different approximations for Eq. (6) can be applied. For the analysis of the scaling behavior in both of these two extremes in the following paragraphs, we assume the electron and ion density to be approximately the same, $\mathcal{N}_e \approx \mathcal{N}_{ion}$, both given by the parameter $\mathcal{N}_c$.

For blue to red detuning sweeps which are described by S in Table I and Fig. 7(b), Δ_E is approximately linear with respect to all three parameters, $(a, b, c) \approx 1$. In order for the system to jump to the plasma state, it is sufficient to trigger the threshold for the avalanche mechanism at a single point along the vapor cell. All traces in Fig. 6(b) feature a sharp edge at the same detuning value. It is important to understand that the Stark shift and associated spectral broadening due to the charge distribution does *not* play a role in this case.

The system starts from the ground state, so we can approximate the rate equations, Eq. (6), as

$$\dot{\mathcal{N}}_c \stackrel{\mathcal{N}_c \ll \mathcal{N}_g}{=} \mathcal{N}_{Ryd}\mathcal{N}_g\sigma_g\overline{v}'' - \mathcal{N}_c\Gamma_t,$$
$$\dot{\mathcal{N}}_{Ryd} \stackrel{\mathcal{N}_c \ll \mathcal{N}_g}{=} -\mathcal{N}_{Ryd}\mathcal{N}_g\sigma_g\overline{v} + \mathcal{N}_g\frac{\Omega_B\Omega_R}{\underset{\sim}{\Delta}}. \quad (7)$$

Here, the pump rate to the Rydberg state is taken to be the effective two-photon Rabi frequency divided by the effective detuning $\underset{\sim}{\Delta}$, making this a nonresonant two-photon coherent excitation. Without the plasma or a significant number of charges, the line width of the Rydberg transition corresponds to its natural width, and both lasers are above saturation. Hence, the Rabi frequencies contribute linearly to the pump rate. In steady state, the charge density from Eq. (7) is given by

$$\mathcal{N}_c \propto \mathcal{N}_g\Omega_B\Omega_R, \quad (8)$$

which reflects the measured linear scaling in all three parameters.

For the opposite scan direction, scaling parameter $S^\star$ in Table I and Fig. 7(a), the dominant terms in Eq. (6) are

$$\dot{\mathcal{N}}_c \stackrel{\mathcal{N}_c \gg 0}{=} \mathcal{N}_{Ryd}\mathcal{N}_c\sigma_e\overline{v} - \mathcal{N}_c^2\sigma_r\overline{v},$$
$$\dot{\mathcal{N}}_{Ryd} \stackrel{\mathcal{N}_c \gg 0}{=} -\mathcal{N}_{Ryd}\mathcal{N}_c\sigma_e\overline{v} + \mathcal{N}_g\frac{\Omega_B}{2\Gamma_D}\frac{\Omega_R^2}{\Gamma_{Ryd}}. \quad (9)$$

With the plasma present, the Rydberg transition is massively broadened by the varying Stark shifts and the 1064-nm laser intensity is effectively *below* the saturation intensity. As a result, the Rydberg population depends quadratically on Ω_R. The 455-nm laser transition remains saturated. The intermediate population is proportional to the Rabi frequency Ω_B divided by the Doppler width Γ_D, reflecting the fact that more velocity classes contribute to the Rydberg population because of the increasing power broadening. Solving Eq. (9) for the steady-state charge density gives

$$\mathcal{N}_c \propto \sqrt{\mathcal{N}_g}\sqrt{\Omega_B}\Omega_R, \quad (10)$$

which is in agreement with the experimentally obtained scaling $S^\star$ shown in Table I. Since both $\mathcal{N}_c$ from our

theoretical considerations and Δ_E from the measurements yield the same scaling behavior, we can conclude that the detuning at which the system undergoes the transition between the two metastable states is proportional to the charge density in the vapor,

$$\Delta_E \propto \mathcal{N}_c. \qquad (11)$$

It is important to note that most of the measurements were not performed in one of the extreme cases mentioned here. Therefore a detailed numerical model is developed in the next section.

V. MICROSCOPIC MODEL

To calculate the state populations and coherences of an ensemble of thermal atoms excited by laser beams, we find the steady-state solution to the Lindblad master equation,

$$\dot{\rho} = -\frac{i}{\hbar}[\rho, H] + L, \qquad (12)$$

for all possible velocities, for a given set of experimental parameters; i.e., a given set of density, laser detuning, and Rabi frequencies. The Rydberg state population, for example, is obtained by averaging over the ensemble weighted by the Boltzmann probability distribution describing the atomic velocities, and the electric field distribution which causes an additional detuning of the Rydberg state due to the Stark shift. Analogous to Doppler averaging, we integrate over the combined probabilities of the electric field and velocity to obtain the observable quantities from the density matrix. Our model of the atomic system is depicted in Figs. 2(a)–2(d).

Applying the density matrix formalism, we describe the thermal gas interacting with the lasers as a conventional $3 + 1$ level system. The lower 3 levels describe the neutral gas including its excitation to the Rydberg state. The additional level ($+1$) describes the generation of ions [Fig. 2(a)] which gives rise to the plasma. Details of the density matrix, the Hamiltonian, and the Lindblad operator, can be found in Appendix B.

We have identified two mechanisms responsible for the ionization of the Rydberg atoms. The ionization rate, which depends on the ion population ρ_{ion}, is given by

$$\Gamma_i(\rho_{\text{ion}}) = \mathcal{N}_g \sqrt{\frac{8k_B T}{\pi}} \left(\sigma_g \sqrt{\frac{2}{m_{\text{Cs}}}} + \sigma_e \frac{\rho_{\text{ion}}}{\sqrt{m_e}} \right), \qquad (13)$$

where m_{Cs} is the mass of a cesium atom. σ_g and σ_e are the ionization cross sections for Rydberg atoms colliding with ground-state atoms [Fig. 2(b)] or electrons [Fig. 2(c)], respectively. Since the ground-state density is not significantly influenced by the excitations, we take $\rho_g \approx 1$ in our model. We assume values for σ_g to be on the order of $0.06\sigma_{\text{geo}}$ [33], with $\sigma_{\text{geo}} = \pi (a_0 n^{\star 2})^2$ being the geometric cross section of the Rydberg state with effective principal quantum number $n^\star$. For σ_e—to our knowledge—there is no literature reference for cesium. However, according to experiments with sodium Rydberg states [41] a reasonable range for this parameter would be $1 - 10\,\sigma_{\text{geo}}$. We neglect that the electron impact ionization cross section depends on the velocity of the electron [42].

In a similar fashion, the rate,

$$\Gamma_d(\rho_{\text{ion}}) = \Gamma_t + \mathcal{N}_g \sqrt{\frac{8k_B T}{\pi m_e}} \sigma_r \rho_{\text{ion}}, \qquad (14)$$

quantifies the mechanisms leading to losses in the charged particle population. The most obvious contribution is charges simply leaving the interaction volume due to their thermal motion which is described by Γ_t. The second term describes recombination of ions with electrons into neutral particles. The transit time losses Γ_t are determined by the diameter of the excitation volume and the velocity of the particles. The measured fluorescence rate can be used to estimate the actual recombination rate, and therefore to determine the recombination cross section σ_r. The expected value for σ_r can be estimated in semiclassical treatment with Kramer's formula [43], which gives a value of $1 \times 10^{-5}\sigma_{\text{geo}}$. However, for the densities shown in the data set in Fig. 8, the approximations in Eq. (7) are not completely valid, and therefore the transit time losses of the ions Γ_t still play a non-negligible role. For even higher charge densities, the neighboring $42D_{3/2}$ is shifted more than the spacing of $2\pi \times 1\text{GHz}$, and starts to overlap with the spectrum of the $42D_{5/2}$ state. Hence, we focused on the parameter space where the two states are still separated. As the distinction between a linear and quadratic component—such as in Eq. (7)—is not feasible in the vicinity of the origin of the plot, c.f. Fig. 7, we reduce the complexity of the model by the following substitution. We replace the recombination term in Eq. (14) with

$$\mathcal{N}_g \sqrt{\frac{8k_B T}{\pi m_e}} \sigma_r \rho_{\text{ion}} = \Gamma_r = \text{const.}, \qquad (15)$$

and thereby assume Γ_d to be an effective ion-loss rate, with a constant value independent of the ion density. We also suppose ions to leave the beam geometry at the same rate Γ_t as Rydberg atoms. Our estimation of the respective rates can be found in Appendix C.

The electric field due to the present charges rapidly varies as the atoms move through the plasma. A distribution of detunings needs to be considered because each atom sees a different sequence of local electric fields, resulting in different accumulated phase shifts. The random distribution of phase shifts can be treated as an effective shift and homogeneous broadening due to dephasing of the Rydberg transition [37]. In our model, we define the overall dephasing factor as

$$\gamma = \gamma_0 + \gamma_S. \qquad (16)$$

$\gamma_0/2\pi = 1\,\text{MHz}$ accounts for the laser line width. The effect of the Stark shift distribution is approximated to be proportional to its weighted mean,

$$\gamma_S = \overline{\Delta_S} = \int_0^\infty dE\, \mathcal{P}_{\mathcal{N}}(E)\Delta_S(E). \qquad (17)$$

The details of the electric field distribution are found in Appendix D.

The fluorescence spectrum is proportional to the square of the charge density ρ_{ion}^2, because of two-body recombination of ions and electrons, and the before mentioned assumption of $\mathcal{N}_e \approx \mathcal{N}_{\text{ion}}$. This process leads to the broad, discrete distribution of Rydberg states which then subsequently emit the
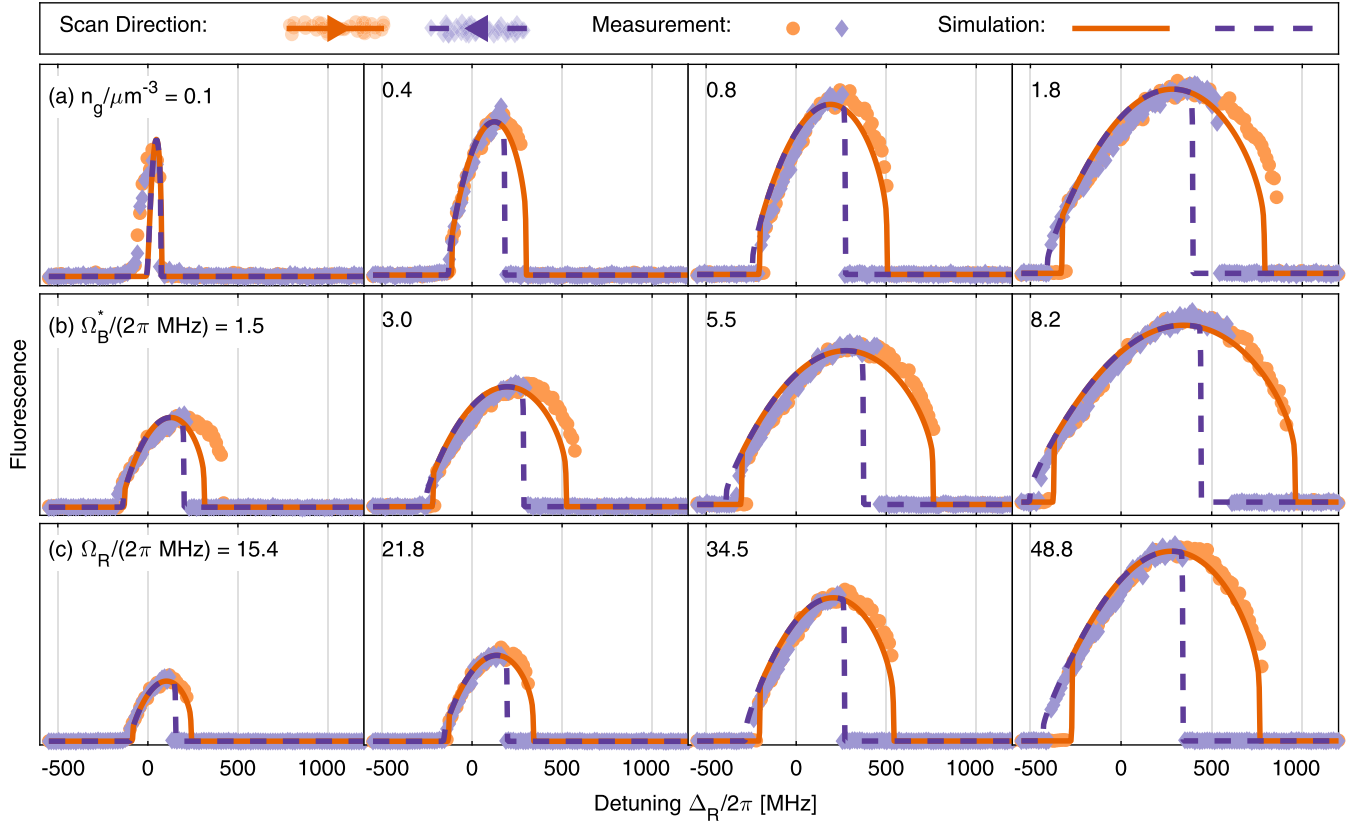
FIG. 8. Comparison between fluorescence obtained as a function of 1064-nm laser detuning and calculations. Each row shows the variation of only one experimental parameter: ground-state atomic density (a), Ω_B (b), and Ω_R (c). The measurement is shown in orange dots (scan from red towards blue wavelengths) and purple diamonds (scan from blue towards red wavelengths). For the simulation we use orange solid and dashed purple lines, respectively. Experimental settings are used as input parameter for the simulation. Only the fluorescence signal amplitude is adjusted to the data. Experimental settings are (a) $\Omega_B/2\pi = 2.6$ MHz, $\Omega_R/2\pi = 15.4$ MHz. (b) $\Omega_R/2\pi = 15.4$ MHz, $\mathcal{N}_g = 1.3 \times 10^{12}$ cm^{-3}. (c) $\Omega_B/2\pi = 5.3$ MHz, $\mathcal{N}_g = 0.2 \times 10^{12}$ cm^{-3}.

fluorescence via their decay. In order to obtain a spectrum to compare to our data, the solution of Eq. (12) for the ion state population of the ensemble of atoms in the vapor cell needs to be calculated. The analytic expressions for the velocity distribution and Stark shift distribution has to be used to average the density matrix elements. The value for a density matrix element for a single laser detuning and charge density is the average of the density matrix element obtained using the respective probability distribution functions for the Stark shifts and the atomic velocities,

$$\overline{\rho}_{i,j} = \int_{-\infty}^{\infty} dv \int_{0}^{\infty} dE \, f(v)\mathcal{P}_{\mathcal{N}}(E)\rho_{i,j}(v,E). \quad (18)$$

$f(v)$ [44] is the one-dimensional Maxwellian distribution function for the velocity v in the beam direction and $P_{\mathcal{N}}(E)$ is the electric field distribution as given in Eq. (D1). In order to obtain an equilibrium solution for the charge density, we make use of an iterative method as described in Appendix E.

We fit the theory to the spectra found in Fig. 8. The parameters that were fit are shown in Table II. We have refined their values via nonlinear least-squares optimization using the Levenberg-Marquardt method [45,46]. The data covered a wide range of different experimental parameters as shown in Fig. 8. We excluded the values close to the plasma formation

edge $\Delta_R > 0$, for the dashed traces. The steep wave form has a disproportionate contribution to the overall error measure, and the point of plasma formation is prone to additional uncertainties, such as fluctuations in charge density due to the cell walls which can trigger the formation of the plasma state. Furthermore, as previously shown in Fig. 7, the edge frequency for the plasma formation point depends on the raw Rabi frequency, while the line shape of the system is defined by the *adjusted* Rabi frequency.

The results of the fits shown in Table II demonstrate that our assumptions are sound, as all the fit values are close to the expected values. Perhaps most significantly, γ_S indicates

TABLE II. Fitted parameter with 95% confidence intervals from the nonlinear least-squares optimization, and expected values derived from other references.

Var.	Fit result	Expect. value	Ref.
Γ_d	$(3.21 \pm 1.55)\Gamma_t$	$2\,\Gamma_t$	Appendix C
γ_S	$(1.69 \pm 1.00)\overline{\Delta_S}$	$1\,\overline{\Delta_S}$	Eq. (17)
σ_g	$(0.04 \pm 0.04)\sigma_{geo}$	$0.06\,\sigma_{geo}$	[33,47]
σ_e	$(1.10 \pm 0.55)\sigma_{geo}$	1 to 10 σ_{geo}	[41]

that our approximation of the line broadening due to the Stark shifts of the plasma is in good agreement with the proposed mechanism. Likewise, Γ_d is consistent with our estimates using the photon emission rate suggesting that our modeling of the recombination rate is consistent with the experimental observations. The cross section σ_g, which accounts for the finite ionization efficiency of Rydberg-ground-state collisions as compared to the geometric cross section σ_{geo}, is in agreement with prior experiments [33], $0.06\sigma_{geo}$ and similar to the very crude estimate in [26], $0.03\sigma_{geo}$. The ionization cross section of the electron-Rydberg collisions, σ_e, also yields a reasonable value. The Coulombic interaction in conjunction with the large polarizability of the Rydberg atom gives an expected cross section that is larger than the geometric cross section [41,48]. Calculating cross sections for the electron-impact ionization of Rydberg states is beyond the scope of this manuscript, but σ_e in Table II is consistent since it is slightly larger than σ_{geo}. Overall, the values that were fit to get best agreement with the spectra are consistent with expected results. From the overall agreement, we conclude that the model is consistent with the spectra.

Figure 8 shows the bistable fluorescence spectra, as captured by the PMT when scanning the 1064-nm laser across the Rydberg resonance line. Because the underlying mechanism is interactions between charged particles and Rydberg atoms, the peak is shifted towards blue detuning as the charge density increases; i.e., more atoms, or higher Rydberg fraction. The shift direction is in agreement with the negative sign of the polarizability one obtains for the $42D_{5/2}$ state [49]. An increase in fluorescence amplitude is also observed as the ground-state density, and consequently the Rydberg density, increases.

The measurements in Fig. 8 are overlaid with the results from the model, adjusted only for amplitude. The solid and dashed lines correspond to positive, red to blue, and negative, blue to red, scan directions, respectively. We achieve excellent agreement between the calculations and the measurements as demonstrated by the low residuals shown in the figure. The spectral broadening and line shape are described well and the hysteresis feature is correctly reproduced for both red and blue 1064-nm detuning sweeps.

For certain settings of laser intensity and ground-state density a second hysteresis feature on the seemingly *wrong* side of the spectrum appears. This has previously been observed [25,26], but is now also straightforward to explain. For a blue-shifting interaction (i.e., addressing a state with a *positive* polarizability [26]), one expects the dominant effect for laser frequencies on the blue detuned side of the resonance. If the spectral broadening is larger than the shift caused by the Stark effect, the far-detuned features of the atom light interaction can extend beyond the original resonance position, and influence the spectrum also on the red detuned side of the overall feature. Nonetheless, the Stark map of the $42D_{5/2}$ state, Fig. 9, features a red shifting branch, and also the $42D_{3/2}$ state is in close proximity. However, both these aspects are neglected in the modeled traces, but the feature is still reproduced correctly.

Despite the overall excellent agreement between the model and experiment, something can be learned from the regions where the deviations are maximum. For one, the plasma

formation point is not always precisely predicted by the simulation for the larger scaling parameters, but the jump occurs earlier than expected. We attribute the deviation to the fact that when the system is in the bistable regime, minor disturbances, e.g., laser fluctuations or random charges produced by the photoelectric effect on the vapor cell walls, can cause the system to jump to the plasma state before reaching a detuning where the jump would take place in the absence of perturbation. Once the system is in the high population state, it will stay there, even if the average parameter values would not support the jump to the plasma state at this point.

VI. CONCLUSION

We have shown measurements and a comprehensive numerical model that describes optical bistability in a thermal Rydberg gas. We showed that plasma formation is the key ingredient in the phenomena of optical bistability in thermal Rydberg gases. By measuring radio-frequency transmission spectra we established that a plasma exists in the gas. We characterized the plasma by direct measurement of the plasma frequency as weakly ionized. Measuring the fluorescence at Δ_E and its dependence on detuning and 1064-nm laser sweep direction allows us to determine the plasma formation point. We combined all experimental parameters into scaling parameters S and S^*, such that the plasma formation point scales linearly with these parameters. The excitation dynamics were characterized using the results. Measuring the fluorescence at different positions along the cell demonstrates the role of absorption of the 455-nm laser. We observed a *lightsaber* like fluorescing beam that extends only along a part of the cell length, because the necessary conditions for the ionization avalanche can only be sustained when the laser is strong enough. The fluorescence spectrum shows a broad range of Rydberg states consistent with recombination from the plasma continuum. We developed a numerical model based on collisional cross sections and motional dephasing in an electric field distribution due to the presence of the plasma, that fits the spectral data extremely well confirming our microscopic model. The physical parameters obtained from fits to the spectral data are in excellent agreement with expectations. We conclude that plasma formation is the fundamental ingredient in optical bistability in thermal Rydberg gases.

APPENDIX A: ADJUSTED RABI FREQUENCIES

The laser beams are being absorbed while propagating through the atomic medium. Therefore, the Rabi frequency in general is a function of the position z, $\Omega = \Omega(z)$, c.f., Fig. 3. In our experiment, the 1064-nm laser intensity is not

considerably affected by absorption along the cell. The blue 455-nm laser beam, however, is strongly absorbed, since it couples the highly populated ground state to the intermediate state. As the *local* Ω_B varies along the length of the vapor cell, the excitation and ionization conditions vary. The spectrum one obtains by measuring the fluorescence therefore depends on the spatial position at which the fluorescence is collected. As a consequence, one needs to adjust Ω_B according to the position where the measurement is made, which is indicated by $\Omega^\star$. We numerically propagate the intensity through a thermal ensemble of the respective density to determine $\Omega^\star$, following the derivation in [50].

APPENDIX B: LINDBLAD MASTER EQUATION

The density matrix is given by

$$\rho = \begin{pmatrix} \rho_g & \rho_{1,2} & \rho_{1,3} & 0 \\ \rho_{2,1} & \rho_{2,2} & \rho_{2,3} & 0 \\ \rho_{3,1} & \rho_{3,2} & \rho_{\text{Ryd}} & 0 \\ 0 & 0 & 0 & \rho_{\text{ion}} \end{pmatrix}, \quad (B1)$$

where the states are coupled by the two lasers according to the Hamiltonian,

$$H = \hbar \begin{pmatrix} 0 & \frac{\Omega_B}{2} & 0 & 0 \\ \frac{\Omega_B}{2} & -\Delta_1 & \frac{\Omega_R}{2} & 0 \\ 0 & \frac{\Omega_R}{2} & -\Delta_1 - (\Delta_2 + \Delta_S) & 0 \\ 0 & 0 & 0 & 0 \end{pmatrix}, \quad (B2)$$

with Rabi frequencies Ω_B and Ω_R and the reduced Planck constant $\hbar$. The detunings are $\Delta_1 = \vec{k}_B \cdot \vec{v}$ and $\Delta_2 = \Delta_R + \vec{k}_R \cdot \vec{v}$ with wave vectors $\vec{k}_B$, $\vec{k}_R$ and atom velocity $\vec{v}$. The detuning Δ_2 includes the laser detuning Δ_R, and the detuning resulting from the Doppler effect. The 455-nm laser is assumed to be tuned to resonance. Figure 2(a) shows the relevant near-resonant atomic levels. In the case of the Rydberg state, the additional term Δ_S represents the Stark shift due to nearby charges, Fig. 2(c). The ground-state and intermediate-state Stark shifts are negligible.

The Lindblad operator, $L = L_1 + L_2 + L_3$ accounts for dephasing, decay, and ionization mechanisms. First, L_1, the intermediate state decoherence and decay, which is dominated by its natural lifetime $\Gamma_{2,1}/2\pi = 1.18\,\text{MHz}$ [51], gives the contribution,

$$L_1 = \begin{pmatrix} \Gamma_{2,1}\rho_{2,2} & -\frac{1}{2}\Gamma_{2,1}\rho_{1,2} & 0 & 0 \\ -\frac{1}{2}\Gamma_{2,1}\rho_{2,1} & -\Gamma_{2,1}\rho_{2,2} & -\Gamma_{2,1}\rho_{2,3} & 0 \\ 0 & -\frac{1}{2}\Gamma_{2,1}\rho_{3,2} & 0 & 0 \\ 0 & 0 & 0 & 0 \end{pmatrix}. \quad (B3)$$

Second, L_2 takes into account ionization and recombination,

$$L_2 = \begin{pmatrix} \Gamma_d\rho_{\text{ion}} & 0 & -\frac{1}{2}\Gamma_i\rho_{1,3} & 0 \\ 0 & 0 & -\frac{1}{2}\Gamma_i\rho_{2,3} & 0 \\ -\frac{1}{2}\Gamma_i\rho_{3,1} & -\frac{1}{2}\Gamma_i\rho_{3,2} & -\Gamma_i\rho_{\text{Ryd}} & 0 \\ 0 & 0 & 0 & \Gamma_i\rho_{\text{Ryd}} - \Gamma_d\rho_{\text{ion}} \end{pmatrix}. \quad (B4)$$

The ionization rates are given by Γ_i while the loss of charged particles due to recombination and motion out of the interaction region are represented by Γ_d.

The interaction between the Rydberg atoms and the plasma is the last part of L and is modeled as

$$L_3 = \begin{pmatrix} \Gamma_{\text{Ryd}}\rho_{\text{Ryd}} & 0 & -\frac{1}{2}\gamma\rho_{1,3} & 0 \\ 0 & 0 & -\frac{1}{2}\gamma\rho_{2,3} & 0 \\ -\frac{1}{2}\gamma\rho_{3,1} & -\frac{1}{2}\gamma\rho_{3,2} & -\Gamma_{\text{Ryd}}\rho_{\text{Ryd}} & 0 \\ 0 & 0 & 0 & 0 \end{pmatrix}. \quad (B5)$$

The rate Γ_{Ryd} includes the natural lifetime of the Rydberg state and transit time effects. The dominating part here clearly is the transit time decay Γ_t, therefore we estimate $\Gamma_{\text{Ryd}}/2\pi = 0.2\,\text{MHz}$ for the beam sizes used in the experiments. The dephasing factor γ accounts for the line broadening mechanisms.

APPENDIX C: RECOMBINATION RATE AND TRANSIT TIME LOSS RATE ESTIMATION

Given the experimental parameters, one can estimate the photon flux emitted by plasma recombination. Here we show the quantitative analysis for the experimental parameters as well as measured and simulated values from the data set in Fig. 8. The atomic densities cover a range from $5 \times 10^{10}\,\text{cm}^{-3}$ to $1.8 \times 10^{12}\,\text{cm}^{-3}$.

The PMT has a sensitivity of $1.89\,\text{VnW}^{-1}$ and yields a signal height of 0.1 to 0.7 V. Given the collection efficiency of the lens system capturing the fluorescence, this corresponds to an emitted power of approximately 70 to 360 nW, or a photon flux of $2 \times 10^{11}\,\text{s}^{-1}$ to $1.1 \times 10^{12}\,\text{s}^{-1}$, when assuming only photons of 600-nm wavelength. The simulation for these configurations, c.f. Sec. V, peaks at a plasma population ρ_{ion} between 0.8×10^{-3} and 9.6×10^{-3}. A sphere with a diameter of 1.5 mm—approximately the volume we collect photons from—therefore contains 4.5×10^5 to 4.8×10^6 ions. Multiplied with the deionization rate reduced by transit time (this
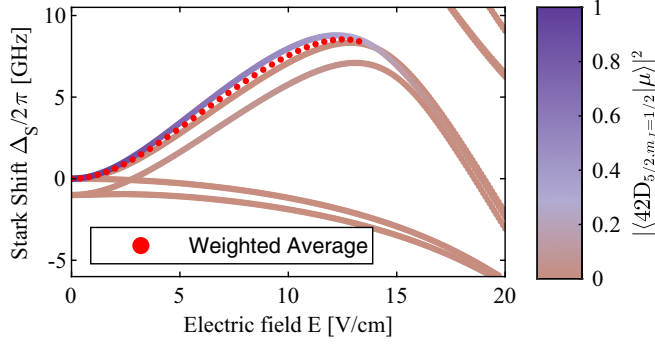
FIG. 9. Stark map for the $42D_{5/2}$ state with all three m_J sublevels, and approximately 1 GHz below the $42D_{3/2}$ state. The overlap to the $42D_{5/2}, m_J = 1/2$ is indicated by the color code for electric field in parallel to the laser polarization. To get an effective mapping from electric field strength to a certain Stark shift, we integrate over all angles for the electric field direction, and weight with the respective overlap to the state the lasers couple to. The dotted line indicates the mapping we used for the Stark shift in our model.

gives the fluorescence photon emission rate), we end up with a total number of 2×10^{11} s^{-1} to 2.1×10^{11} s^{-1}, which is in excellent agreement with the measured photon flux. The simulated Rydberg population ranges between 2.1×10^8 cm^{-3} and 2.5×10^8 cm^{-3}, which is around 4×10^5 Rydberg excitations per 1.5-mm sphere.

With regard to the transit time losses, we estimate $\Gamma_t/2\pi = 0.2$ MHz for the given beam sizes. By multiplying the rate with the ion numbers per 1.5-mm sphere from above, we obtain values for the transit time ion loss between 9×10^{10} s^{-1} and 9.7×10^{11} s^{-1}, roughly the same range as the photon flux.

APPENDIX D: ELECTRIC FIELD DISTRIBUTION

The interesting part of the fluorescence spectrum for the $42D_{5/2}$ Rydberg state occurs on the blue detuned side of the Rydberg resonance, where the plasma suddenly forms. A Stark map for the $42D_{5/2}$ Rydberg state, calculated using [52], is shown in Fig. 9. The particular state has three sublevels and splits up into two branches. The dominant branch has a negative polarizability, and consists of $m_J = 1/2$ and $3/2$. The second branch, $m_J = 5/2$, evokes a red detuning Stark shift. Since the electric field caused by randomly positioned charges has no preferred direction, we integrate over all angles with respect to the laser polarization axis. The dominant contribution to the Stark shift for each electric field strength is then obtained via the angular integral, weighted by the respective overlap with the (unperturbed) $42D_{5/2}, m_J = 1/2$ state. Since both positive and negative branches are well separated for most of the electric field strengths, we only consider the blue-shifting branch for our calculations.

The electric field distribution is modeled by randomly positioned point charges which depends on the charge density $\mathcal{N}$. The distribution, $\mathcal{P}_\mathcal{N}(E)$, is described by the Holtsmark probability distribution function [36],

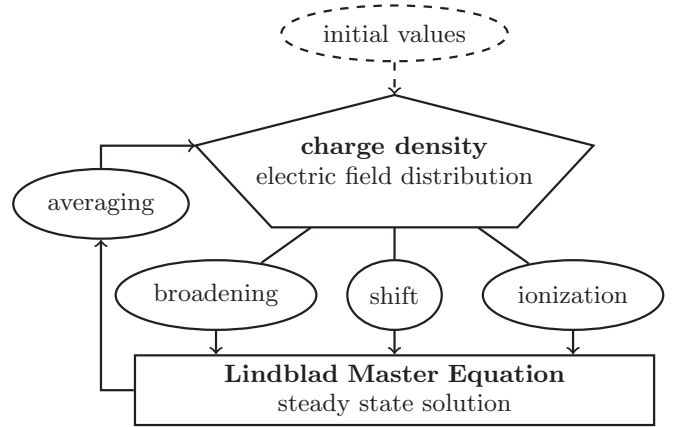$$\mathcal{P}_\mathcal{N}(E) = \mathcal{H}(E/Q_\mathcal{H})/Q_\mathcal{H}, \tag{D1}$$

FIG. 10. Flow chart of the algorithm. At each iteration, the current charge density determines an electric field distribution and hence the broadening and shift of the Rydberg energy level. The charge density also influences the ionization rate. With these values, the ensemble of steady-state solutions of the master equation is calculated. When averaged over all velocity and electric field components, an improved estimation of the charge density at each laser detuning is achieved. The procedure is repeated until the system converges to a steady-state solution.

where the normal field is given by

$$Q_\mathcal{H} = \frac{e}{2\epsilon_0} \left(\frac{4}{15}\mathcal{N}\right)^{\frac{2}{3}}, \tag{D2}$$

and

$$\mathcal{H}(\beta) = \frac{2}{\pi\beta} \int_0^\infty \mathrm{d}x\, x \sin(x) \exp\left(-(x/\beta)^{3/2}\right). \tag{D3}$$

The electric field strengths E are converted into Rydberg energy level shifts via the angular average of the Stark map for the Rydberg state, as calculated in the previous paragraph. We used only the ion density for the electric field distribution calculations. The electrons move much faster than ions, and the energy shifts due to their electric fields averages out on a time scale that is shorter than the atomic dynamics.

APPENDIX E: ITERATIVE EQUILIBRIUM

For a given initial charge density, Ω_B, Ω_R, atomic density, temperature, and Stark shift distribution, a steady-state solution of the master equation is obtained that yields a charge density,

$$\mathcal{N}' = \rho_{\mathrm{ion}}\mathcal{N}_{\mathrm{g}}. \tag{E1}$$

The calculated charge density is used for a subsequent calculation. The equations are solved iteratively using the previous calculation of the charge density as an input parameter for subsequent computation steps until the system converges to an equilibrium solution. A flow chart summarizing this algorithm is shown in Fig. 10.

[1] M. Saffman and T. G. Walker, Analysis of a quantum logic device based on dipole-dipole interactions of optically trapped Rydberg atoms, Phys. Rev. A **72**, 022347 (2005).

[2] M. P. A. Jones, J. Beugnon, A. Gaëtan, J. Zhang, G. Messin, A. Browaeys, and P. Grangier, Fast quantum state control of a single trapped neutral atom, Phys. Rev. A **75**, 040301(R) (2007).

[3] R. Löw, H. Weimer, U. Krohn, R. Heidemann, V. Bendkowsky, B. Butscher, H. P. Büchler, and T. Pfau, Universal scaling in a strongly interacting Rydberg gas, Phys. Rev. A **80**, 033422 (2009).

[4] P. Schauß, J. Zeiher, T. Fukuhara, S. Hild, M. Cheneau, T. Macrì, T. Pohl, I. Bloch, and C. Groß, Crystallization in Ising quantum magnets, Science **347**, 1455 (2015).

[5] Y. Dudin and A. Kuzmich, Strongly interacting Rydberg excitations of a cold atomic gas, Science **336**, 887 (2012).

[6] T. Peyronel, O. Firstenberg, Q.-Y. Liang, S. Hofferberth, A. V. Gorshkov, T. Pohl, M. D. Lukin, and V. Vuletić, Quantum nonlinear optics with single photons enabled by strongly interacting atoms, Nature (London) **488**, 57 (2012).

[7] D. Maxwell, D. J. Szwer, D. Paredes-Barato, H. Busche, J. D. Pritchard, A. Gauguet, K. J. Weatherill, M. P. A. Jones, and C. S. Adams, Storage and Control of Optical Photons Using Rydberg Polaritons, Phys. Rev. Lett. **110**, 103001 (2013).

[8] D. Tiarks, S. Baur, K. Schneider, S. Dürr, and G. Rempe, Single-Photon Transistor Using a Förster Resonance, Phys. Rev. Lett. **113**, 053602 (2014).

[9] H. Gorniaczyk, C. Tresp, J. Schmidt, H. Fedder, and S. Hofferberth, Single-Photon Transistor Mediated by Interstate Rydberg Interactions, Phys. Rev. Lett. **113**, 053601 (2014).

[10] R. Faoro, B. Pelle, A. Zuliani, P. Cheinet, E. Arimondo, and P. Pillet, Borromean three-body FRET in frozen Rydberg gases, Nat. Commun. **6**, 8173 (2015).

[11] G. Günter, H. Schempp, M. Robertde SaintVincent, V. Gavryusev, S. Helmrich, C. Hofmann, S. Whitlock, and M. Weidemüller, Observing the dynamics of dipole-mediated energy transport by interaction-enhanced imaging, Science **342**, 954 (2013).

[12] D. Barredo, H. Labuhn, S. Ravets, T. Lahaye, A. Browaeys, and C. S. Adams, Coherent Excitation Transfer in a Spin Chain of Three Rydberg Atoms, Phys. Rev. Lett. **114**, 113002 (2015).

[13] H. Schempp, G. Günter, M. Robertde SaintVincent, C. S. Hofmann, D. Breyel, A. Komnik, D. W. Schönleber, M. Gärttner, J. Evers, S. Whitlock, and M. Weidemüller, Full Counting Statistics of Laser Excited Rydberg Aggregates in a One-Dimensional Geometry, Phys. Rev. Lett. **112**, 013002 (2014).

[14] N. Malossi, M. M. Valado, S. Scotto, P. Huillery, P. Pillet, D. Ciampini, E. Arimondo, and O. Morsch, Full Counting Statistics and Phase Diagram of a Dissipative Rydberg Gas, Phys. Rev. Lett. **113**, 023006 (2014).

[15] A. Urvoy, F. Ripka, I. Lesanovsky, D. Booth, J. P. Shaffer, T. Pfau, and R. Löw, Strongly Correlated Growth of Rydberg Aggregates in a Vapor Cell, Phys. Rev. Lett. **114**, 203002 (2015).

[16] V. Bendkowsky, B. Butscher, J. Nipper, J. P. Shaffer, R. Löw, and T. Pfau, Observation of ultralong-range rydberg molecules, Nature (London) **458**, 1005 (2009).

[17] K. R. Overstreet, A. Schwettmann, J. Tallant, D. Booth, and J. P. Shaffer, Observation of electric-field-induced cs Rydberg atom macrodimers, Nat. Phys. **5**, 581 (2009).

[18] J. A. Sedlacek, A. Schwettmann, H. Kübler, and J. P. Shaffer, Atom-Based Vector Microwave Electrometry Using Rubidium Rydberg Atoms in a Vapor Cell, Phys. Rev. Lett. **111**, 063001 (2013).

[19] C. G. Wade, M. Marcuzzi, E. Levi, J. M. Kondo, I. Lesanovsky, C. S. Adams, and K. J. Weatherill, A terahertz-driven nonequilibrium phase transition in a room temperature atomic vapour, Nat. Commun. **9**, 3567 (2018).

[20] F. Ripka, H. Kübler, R. Löw, and T. Pfau, A room-temperature single-photon source based on strongly interacting Rydberg atoms, Science **362**, 446 (2018).

[21] C. Carr, R. Ritter, C. G. Wade, C. S. Adams, and K. J. Weatherill, Nonequilibrium Phase Transition in a Dilute Rydberg Ensemble, Phys. Rev. Lett. **111**, 113901 (2013).

[22] M. Marcuzzi, E. Levi, S. Diehl, J. P. Garrahan, and I. Lesanovsky, Universal Nonequilibrium Properties of Dissipative Rydberg Gases, Phys. Rev. Lett. **113**, 210401 (2014).

[23] N. Šibalić, C. G. Wade, C. S. Adams, K. J. Weatherill, and T. Pohl, Driven-dissipative many-body systems with mixed power-law interactions: Bistabilities and temperature-driven nonequilibrium phase transitions, Phys. Rev. A **94**, 011401(R) (2016).

[24] N. R. de Melo, C. G. Wade, N. Šibalić, J. M. Kondo, C. S. Adams, and K. J. Weatherill, Intrinsic optical bistability in a strongly driven Rydberg ensemble, Phys. Rev. A **93**, 063863 (2016).

[25] D.-S. Ding, C. S. Adams, B.-S. Shi, and G.-C. Guo, Nonequilibrium phase-transitions in multi-component Rydberg gases, arXiv:1606.08791v1.

[26] D. Weller, A. Urvoy, A. Rico, R. Löw, and H. Kübler, Charge-induced optical bistability in thermal Rydberg vapor, Phys. Rev. A **94**, 063820 (2016).

[27] P. Siddons, C. S. Adams, C. Ge, and I. G. Hughes, Absolute absorption on rubidium d lines: Comparison between theory and experiment, J. Phys. B **41**, 155004 (2008).

[28] K. L. Corwin, Z.-T. Lu, C. F. Hand, R. J. Epstein, and C. E. Wieman, Frequency-stabilized diode laser with the Zeeman shift in an atomic vapor, Appl. Opt. **37**, 3295 (1998).

[29] P. Fritschel, A. Jeffries, and T. J. Kane, Frequency fluctuations of a diode-pumped nd: Yag ring laser, Opt. Lett. **14**, 993 (1989).

[30] A. K. Mohapatra, T. R. Jackson, and C. S. Adams, Coherent Optical Detection of Highly Excited Rydberg States Using Electromagnetically Induced Transparency, Phys. Rev. Lett. **98**, 113003 (2007).

[31] P. R. Bowden, It's all about energy, Phys. World **29**, 64 (2016).

[32] F. Letscher, O. Thomas, T. Niederprüm, M. Fleischhauer, and H. Ott, Bistability Versus Metastability in Driven Dissipative Rydberg Gases, Phys. Rev. X **7**, 021020 (2017).

[33] G. Vitrant, J. Raimond, M. Gross, and S. Haroche, Rydberg to plasma evolution in a dense gas of very excited atoms, J. Phys. B **15**, L49 (1982).

[34] T. C. Killian, S. Kulin, S. D. Bergeson, L. A. Orozco, C. Orzel, and S. L. Rolston, Creation of an Ultracold Neutral Plasma, Phys. Rev. Lett. **83**, 4776 (1999).

[35] M. P. Robinson, B. Laburthe Tolra, M. W. Noel, T. F. Gallagher, and P. Pillet, Spontaneous Evolution of Rydberg Atoms into an Ultracold Plasma, Phys. Rev. Lett. **85**, 4466 (2000).

[36] J. Holtsmark, Über die verbreiterung von spektrallinien, Ann. Phys. **363**, 577 (1919).

[37] C. Lin, C. Gocke, G. Röpke, and H. Reinholz, Transition rates for a Rydberg atom surrounded by a plasma, Phys. Rev. A **93**, 042711 (2016).

[38] L. Agnew and W. Reichelt, Identification of the ionic species in a cesium plasma diode, J. Appl. Phys. **39**, 3149 (1968).

[39] R. Schunk and A. Nagy, *Ionospheres: Physics, Plasma Physics, and Chemistry* (Cambridge University Press, Cambridge, 2009).

[40] High Rydberg density implies high charge density.

[41] K. Nagesha and K. B. MacAdam, Electron Impact Ionization of Sodium Rydberg Atoms Below 2 eV, Phys. Rev. Lett. **91**, 113202 (2003).

[42] D. Vrinceanu, Electron impact ionization of Rydberg atoms, Phys. Rev. A **72**, 022722 (2005).

[43] H. A. Kramers, XCIII. On the theory of X-ray absorption and of the continuous X-ray spectrum, The London, Edinburgh, and Dublin Phil. Mag. J. Sci. **46**, 836 (1923).

[44] J. C. Maxwell, V. Illustrations of the dynamical theory of gases. Part I. On the motions and collisions of perfectly elastic spheres, The London, Edinburgh, and Dublin Phil. Mag. J. Sci. **19**, 19 (1860).

[45] K. Levenberg, A method for the solution of certain non-linear problems in least squares, Q. Appl. Math. **2**, 164 (1944).

[46] D. W. Marquardt, An algorithm for least-squares estimation of nonlinear parameters, J. Soc. Ind. Appl. Math. **11**, 431 (1963).

[47] S. Kumar, H. Fan, H. Kübler, J. Sheng, and J. P. Shaffer, Atom-based sensing of weak radio frequency electric fields using homodyne readout, Sci. Rep. **7**, 42981 (2017).

[48] H. Deutsch, K. MacAdam, K. Becker, H. Zhang, and T. Märk, Calculated cross sections for the electron-impact ionization of na (ns) and na (nd) Rydberg atoms, J. Phys. B **39**, 343 (2005).

[49] N. Šibalić, J. D. Pritchard, C. S. Adams, and K. J. Weatherill, Arc: An open-source library for calculating properties of alkali Rydberg atoms, Comput. Phys. Commun. **220**, 319 (2017).

[50] P. Siddons, Light propagation through atomic vapours, J. Phys. B **47**, 093001 (2014).

[51] R. W. Schmieder, A. Lurio, W. Happer, and A. Khadjavi, Level-crossing measurement of lifetime and hfs constants of the p 3 2 2 states of the stable alkali atoms, Phys. Rev. A **2**, 1216 (1970).

[52] S. Weber, C. Tresp, H. Menke, A. Urvoy, O. Firstenberg, H. P. Büchler, and S. Hofferberth, Calculation of Rydberg interaction potentials, J. Phys. B **50**, 133001 (2017).